



A Noncorotating Gas Component in an Extreme Starburst at $z = 4.3$

Ken-ichi Tadaki¹, Daisuke Iono^{1,2}, Min S. Yun³, Itziar Aretxaga⁴, Bunyo Hatsukade⁵, Minju M. Lee⁶,
Tomonari Michiyama¹, Kouichiro Nakanishi^{1,2}, Toshiki Saito⁷, Junko Ueda¹, and Hideki Umehata^{5,8}

¹National Astronomical Observatory of Japan, 2-21-1 Osawa, Mitaka, Tokyo 181-8588, Japan; tadaki.ken@nao.ac.jp

²Department of Astronomical Science, SOKENDAI (The Graduate University for Advanced Studies), Mitaka, Tokyo 181-8588, Japan

³Department of Astronomy, University of Massachusetts, Amherst, MA 01003, USA

⁴Instituto Nacional de Astrofísica, Óptica y Electrónica (INAOE), Puebla, Mexico

⁵Institute of Astronomy, Graduate School of Science, The University of Tokyo, 2-21-1 Osawa, Mitaka, Tokyo 181-0015, Japan

⁶Max-Planck-Institut für extraterrestrische Physik (MPE), Giessenbachstr., D-85748 Garching, Germany

⁷Max-Planck Institute for Astronomy, Königstuhl, 17 D-69117 Heidelberg, Germany

⁸RIKEN Cluster for Pioneering Research, 2-1 Hirosawa, Wako-shi, Saitama 351-0198, Japan

Received 2019 June 19; revised 2019 December 16; accepted 2019 December 23; published 2020 February 3

Abstract

We report the detection of a noncorotating gas component in a bright unlensed submillimeter galaxy at $z = 4.3$, hosting a compact starburst. Atacama Large Millimeter/submillimeter Array 0''17 and 0''09 resolution observations of [C II] emission clearly demonstrate that the gas kinematics are characterized by an ordered rotation. After subtracting the best-fit model of a rotating disk, we kinematically identify two residual components in the channel maps. Both observing simulations and analysis of dirty images confirm that these two subcomponents are not artificially created by noise fluctuations and beam deconvolution. One of the two has a velocity offset of 200 km s^{-1} and a physical separation of 2 kpc from the primary disk and is located along the kinematic minor axis of disk rotation. We conclude that this gas component is falling into the galaxy from a direction perpendicular to the disk rotation. The accretion of such small noncorotating gas components could stimulate violent disk instability, driving radial gas inflows into the center of galaxies and leading to formation of in situ clumps such as identified in dust continuum and CO. We require more theoretical studies on high gas fraction mergers with mass ratio of $1: > 10$ to verify this process.

Key words: galaxies: evolution – galaxies: high-redshift – galaxies: ISM

1. Introduction

Bright submillimeter galaxies (SMGs) are intensively forming stars with a rate of $1000 M_{\odot} \text{ yr}^{-1}$, except for strongly lensed objects. The dust continuum emission is compact with a half-light radius of ~ 1 kpc (e.g., Ikarashi et al. 2015; Simpson et al. 2015; Hodge et al. 2016), which corresponds to the size of a bulge in massive quiescent galaxies at $z \sim 2$ and giant elliptical galaxies at $z = 0$ (e.g., Daddi et al. 2005; Trujillo et al. 2006; Damjanov et al. 2011; van Dokkum et al. 2015). These findings suggest an evolutionary link between bright SMGs and compact quiescent galaxies at $z \sim 2$ (Toft et al. 2014), although it is not necessarily the case in faint SMGs with a flux density of < 3.5 mJy at $850 \mu\text{m}$ (Valentino et al. 2019). The star-formation rate surface density in the central 1–2 kpc region exceeds $100 M_{\odot} \text{ yr}^{-1} \text{ kpc}^{-2}$ (e.g., Younger et al. 2008; Casey et al. 2014; Tadaki et al. 2018). Understanding the physical mechanism triggering such an extreme starburst in early universe is a main topic in this paper.

In the hierarchical structure formation scenario, galaxies build up their stellar mass, morphology, and angular momentum through multiple-mergers (e.g., Hayward et al. 2013). Major mergers with a mass ratio from 1:1 to 1:4 drive gas inflows into the center, leading to a nuclear starburst as well as feeding a supermassive black hole in the center of a galaxy (e.g., Hopkins et al. 2006). In local universe, extreme starburst galaxies with a total infrared luminosity of $L_{\text{IR}} > 10^{11.8} L_{\odot}$ are all associated with an equal-mass companion with a separation of less than 10 kpc (e.g., Sanders et al. 1988; Larson et al. 2016). Although some CO or [C II] line observations of high-redshift SMGs identify gas-rich companions with a separation

of 30–200 kpc (e.g., Tacconi et al. 2008; Daddi et al. 2009; Ivison et al. 2012, 2013; Riechers et al. 2014), there is not clear evidence that they are in a late-stage of major mergers or in the final coalescence where the star-forming activity is the most enhanced. Parsec-resolution hydrodynamical numerical simulations demonstrate that major mergers of galaxies with a high gas fraction of 60% are less efficient at producing starbursts compared to mergers with a low gas fraction of 10%, expected at low-redshift (Fensch et al. 2017). Even if high-redshift SMGs experience a major merger, it could not necessarily trigger an extreme starburst.

Minor mergers with a mass ratio of 1:10 are expected to happen more frequently (e.g., Lin et al. 2004; Jogee et al. 2009; Kaviraj et al. 2009) and contribute to enhancements in star-formation activity (e.g., Kaviraj 2014; Starkenburg et al. 2016). The accretion of small satellites onto massive galaxies could also affect the dynamical condition and cause compaction of the gas disk if the gas fractions of the companions are high (e.g., Dekel et al. 2009; Zolotov et al. 2015). However, late-stage minor mergers are poorly explored in observations of high-redshift SMGs because it is difficult to identify small companions at a distance of less than 10 kpc ($< 1''5$) due to limitations of sensitivity and spatial resolution in submillimeter/millimeter observations.

Recent high-resolution observations have revealed off-center gas clumps in SMGs and dusty star-forming galaxies (e.g., Hodge et al. 2012; Aravena et al. 2014; Iono et al. 2016; Hodge et al. 2019; Rujopakarn et al. 2019). The gas mass surface densities are extremely high, $\Sigma_{\text{gas}} \sim 10^4 M_{\odot} \text{ pc}^{-2}$, in the central 1–2 kpc region and then the self-gravity of the gas overcomes the internal pressure due to stellar-radiation

feedback with Toomre Q parameters of $Q < 1$ (e.g., Genzel et al. 2011; De Breuck et al. 2014; Swinbank et al. 2015; Tadaki et al. 2018; Litke et al. 2019). Off-center clumps are therefore expected to be formed through the gravitational instability of the dense gas disk. On the other hand, they potentially have an ex situ origin such as late-stage minor mergers. In this paper, we report the detection of a noncorotating subcomponent in a bright SMG at $z = 4.3$, COSMOS-AzTEC-1, from deep and high-resolution Atacama Large Millimeter/submillimeter Array (ALMA) observations of $860 \mu\text{m}$ continuum and [C II] line emission.

2. Data

We use data sets from ALMA Band-7 observations of COSMOS-AzTEC-1 with a central frequency of 350 GHz ($860 \mu\text{m}$), conducted in two array configurations (Iono et al. 2016; Tadaki et al. 2019). The compact and extended configuration observations cover the baseline lengths of 15 m–2.5 km and 178 m–14.6 km, respectively. The integration time is ~ 30 minutes in both configurations. We calibrate the data in the standard manner using CASA (McMullin et al. 2007). There is no systematic offset in the amplitude of the vector-averaged visibilities between the compact and extended configuration data (Appendix A).

First, we make a high-resolution $860 \mu\text{m}$ continuum map by combining the two configuration data. We use only two spectral windows because the other two detect [C II] $158 \mu\text{m}$ and OH $163 \mu\text{m}$ emission lines. We decrease the absolute visibility weights of the compact data by 0.2, and then combine the two configuration data in the visibility plane using the CASA/concat task. Cleaning with weighting of `robust = +2.0` and `uvtaper = 0''05` results in a spatial resolution of $0''09 \times 0''09$ with reasonable sidelobe levels. We clean the map down to the 1σ level in a circular mask with a diameter of $1''$ using the CASA/tclean task. We also adopt Multi-Scale Clean algorithm (Cornwell 2008) to detect extended uncleaned emission in the smoothed residual images. We estimate the noise level by calculating the root mean square and the standard deviation about the mean in the annular region between radii of $1''$ and $9''$, corresponding to the primary beam size of the clean map. These two measurements are identical, resulting in the noise level of $46 \mu\text{Jy beam}^{-1}$.

Next, we make low- and high-resolution clean cubes with a channel width of 30 km s^{-1} for studying the [C II] emission line in COSMOS-AzTEC-1. We simply combine the two configuration data without decreasing the absolute visibility weights and create a low-resolution cube with the parameters of `robust = +2.0` and `uvtaper = 0''1`, resulting in a spatial resolution of $0''17 \times 0''16$. The noise levels in the low- and high-resolution cubes are $0.40 \text{ mJy beam}^{-1}$ per channel and $0.45 \text{ mJy beam}^{-1}$ per channel, respectively. We make [C II] maps of velocity-integrated flux, velocity field, and velocity dispersion in the velocity range between -240 and $+240 \text{ km s}^{-1}$ using the CASA/immoments task (Figure 1). Both of the low- and high-resolution velocity maps show a clear sign of rotation with a monotonic gradient from southeast to northwest.

3. Analysis

Previous $0''05$ -resolution $860 \mu\text{m}$ continuum map reveals that COSMOS-AzTEC-1 is composed of a central starburst disk and multiple off-center clumps (Iono et al. 2016). We

identify clump candidates by using the new dust continuum map and [C II] line cube. In both cases, we first fit disk models to the data and then search for the residual emission in the model-subtracted images.

3.1. Clump Identification in Dust Continuum Emission

To extract the primary disk component, we fit single Sérsic models to the high-resolution $860 \mu\text{m}$ map using the GALFIT code (Peng et al. 2010). We use a clean Gaussian beam as a point-spread function for deconvolution. There are seven free parameters of the models: centroid position (x, y) , $860 \mu\text{m}$ continuum flux density S_{860} , half-light radius $R_{1/2}$, Sérsic index n ($n = 0.5$ for Gaussian, $n = 1$ for an exponential profile, $n = 4$ for de Vaucouleurs profile), minor-to-major axis ratio q , and position angle while the sky value is fixed to be zero. We obtain the best-fit model of the primary disk component with fitting errors of 1% or less (Figure 2). On the other hand, simulations of ALMA observations indicate that there are much larger systematic and random errors in the measurements (3%–10%; see Appendix B). We take into account these errors but note that they do not include uncertainties due to differences between real galaxies and idealized profiles (Peng et al. 2010). We derive $S_{860} = 17.50 \pm 0.74 \text{ mJy}$, $R_{1/2} = 1.22 \pm 0.07 \text{ kpc}$, $n = 1.26 \pm 0.09$ and $q = 0.64 \pm 0.02$, which are consistent with the previous results showing that the morphology of dust emission is characterized by a compact exponential disk (Hodge et al. 2016; Fujimoto et al. 2018). In the residual map after subtracting the Sérsic disk, we detect the emission at 5σ in several regions as well as negative 5σ emission (Figure 2). Iono et al. (2016) previously identified 11 clumps at above 4σ and 3 out of 11 (dust clump-1, -2, -3) are detected at above 5σ . The two high signal-to-noise ratio (S/N) clumps (dust clump-2 and dust clump-3) are identified at 9.7σ and 10.6σ in the residual map from this analysis, respectively. These bright clumps are likely to pull the central position of the best-fit models toward south, possibly causing the central residual emission and negative residuals around the center. As the brightest dust clump (dust clump-1) is very close to the nuclei, it seems to be hard to isolate this clump even at $0''09$ resolution. On the other hand, the other eight low S/N (4 – 5σ) clumps were not detected in the residual map. The extended configuration data presented in Iono et al. (2016) was only observed for a short ~ 30 minutes on-source time and has relatively sparse uv coverage especially at the longer baselines. This can possibly lead to low S/N artifacts in the map, and the true spatial distribution can only be revealed by obtaining a better uv coverage with longer on-source integration time. We caution that low S/N off-center clumps could be misidentified due to noise fluctuations on a smooth disk. Hodge et al. (2016) show by observing simulations that smooth exponential disks break up into a few clumps. It is therefore important to subtract the smooth component before identifying clumps so that we can avoid artifacts associated to the noises.

To take into account two bright off-center clumps, we remake the fitting using three component models, which consist of a single Sérsic profile for the primary disk and two point sources for dust clump-2 and dust clump-3. We derive $S_{860} = 15.99 \pm 0.45 \text{ mJy}$, $R_{1/2} = 1.13 \pm 0.05 \text{ kpc}$, $n = 1.47 \pm 0.10$, and $q = 0.66 \pm 0.02$ for the primary disk, $S_{860} = 0.67 \pm 0.08 \text{ mJy}$ for dust clump-2, and $S_{860} = 0.70 \pm 0.08 \text{ mJy}$ for dust clump-3. The total flux density is $S_{860} = 17.36 \pm 0.46 \text{ mJy}$. After subtracting the best-fit model, the residual map still shows a

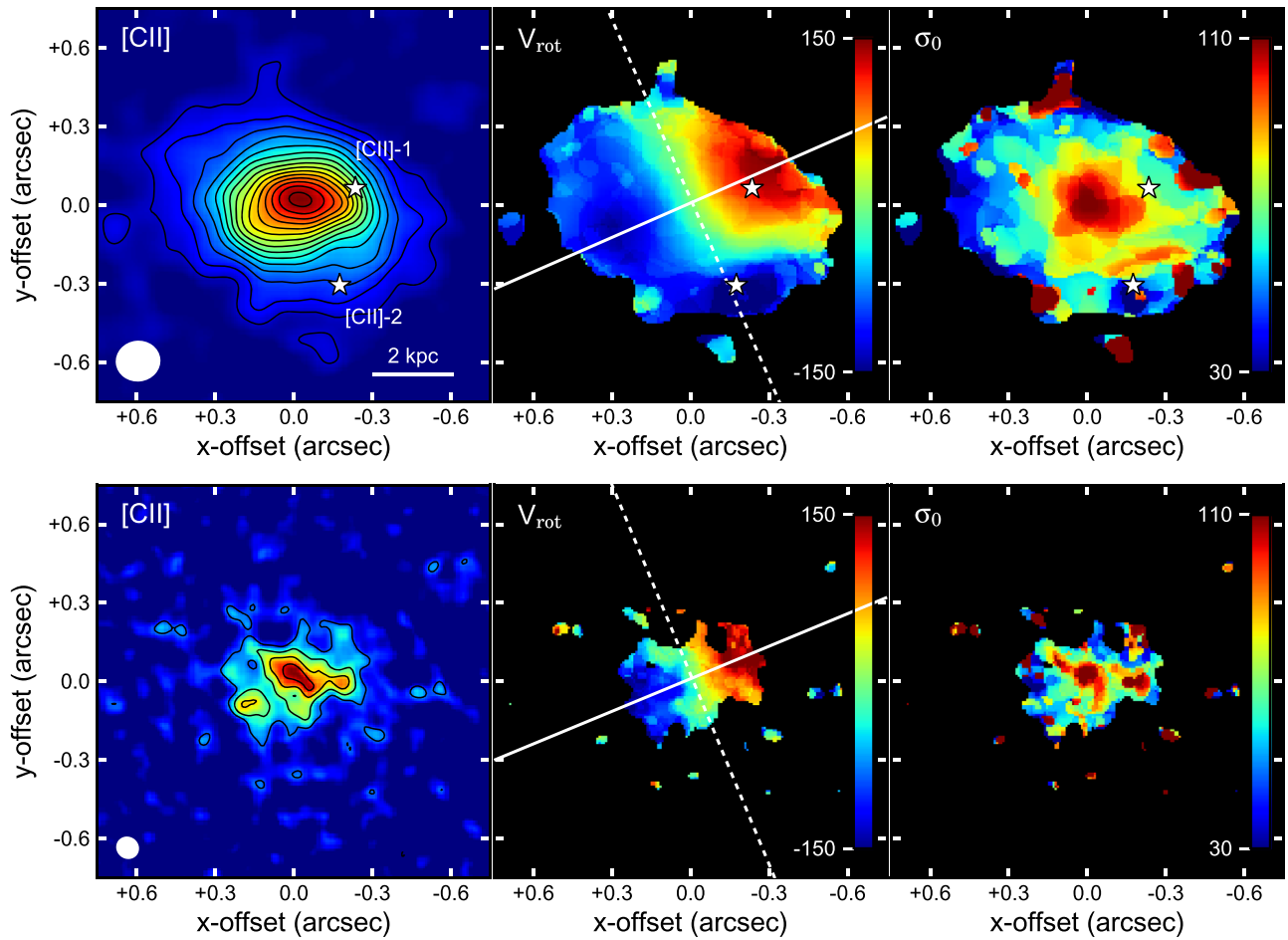


Figure 1. Low-resolution ($0''.17$; top panels) and high-resolution ($0''.09$; bottom panels) ALMA images of [C II] line emission. From left to right, we show the velocity-integrated flux maps, the line-of-sight velocity maps and local velocity dispersion maps. White solid and dashed lines show the kinematic major and minor axis of disk rotation, respectively. White stars mark the positions of [C II] subcomponents (Section 3.2). Contours are plotted every 2σ from 3σ .

6.7σ peak (Figure 2). Simulations of ALMA observations demonstrate that $>6\sigma$ peaks are not artificially created by instrumental noise, contributions due to imperfect uv sampling, and noise fluctuations on the underlying smooth disk (see Appendix B). The residual component is likely to be a real substructure while it does not necessarily mean an independent clump from the disk. Therefore we adopt a more strict criterion that residual emission is detected above 7σ for identifying off-center clumps.

The deep high-resolution $860\ \mu\text{m}$ map allows us not only to identify off-center clumps but also to constrain the spatial extent of the dust emission. We here assume that off-center clumps are spatially extended and have a circular Gaussian shape, characterized by flux density and half-light radius. Then, we fit three component models (Sérsic plus two Gaussians) to the high-resolution $860\ \mu\text{m}$ map (Figure 2). We derive $S_{860} = 13.62 \pm 0.69$ mJy, $R_{1/2} = 1.04 \pm 0.08$ kpc, $n = 1.58 \pm 0.14$ and $q = 0.65 \pm 0.03$ for the disk, $S_{860} = 2.09 \pm 0.31$ mJy and $R_{1/2} = 0.54 \pm 0.06$ kpc for dust clump-2 and $S_{860} = 1.38 \pm 0.18$ mJy and $R_{1/2} = 0.38 \pm 0.05$ kpc for dust clump-3. The total flux density is $S_{860} = 17.09 \pm 0.78$ mJy. The size of these dust clumps is much larger than that of giant molecular clouds in the Milky Way and nearby galaxies (e.g., Bolatto et al. 2008; Heyer & Dame 2015) but is comparable to that of clumps identified in local and high-redshift star-forming galaxies (e.g., Elmegreen & Elmegreen 2005; Newman et al. 2012; Fisher et al. 2017). Dust

clump-2 and dust clump-3 contribute 12% and 8% to the total $860\ \mu\text{m}$ flux density, respectively.

We find that the derived total $860\ \mu\text{m}$ flux densities are consistent within the errors among the three models. It would also make sense that clump flux densities in the Gaussian model become larger than those in the point-source model because extended clumps get more flux density from the disk component. The extended model results in better fitting and well reproduces the overall distribution of dust continuum emission. On the other hand, the local distribution around the clumps more resembles the point-source model, suggesting the possibility that the clumps are more compact than estimated from the Gaussian model. The eastern residual component makes fitting of the three component model difficult. Adding more components to models is one way to more accurately assess the complex distribution whether it is a part of the disk or an independent clump.

3.2. Residual Components in [C II] Line Emission

Next, we search for residual components in [C II] emission after subtracting the disk component. Figure 3 shows the low-resolution channel maps of the [C II] emission. The maximum $S/N = 17$ in a channel of $-135\ \text{km s}^{-1}$ while the significance of the peak decreases to $S/N = 7$ in the high-resolution channel maps. Therefore, we use the low-resolution [C II] cube for identifying residual components. We fit kinematic models

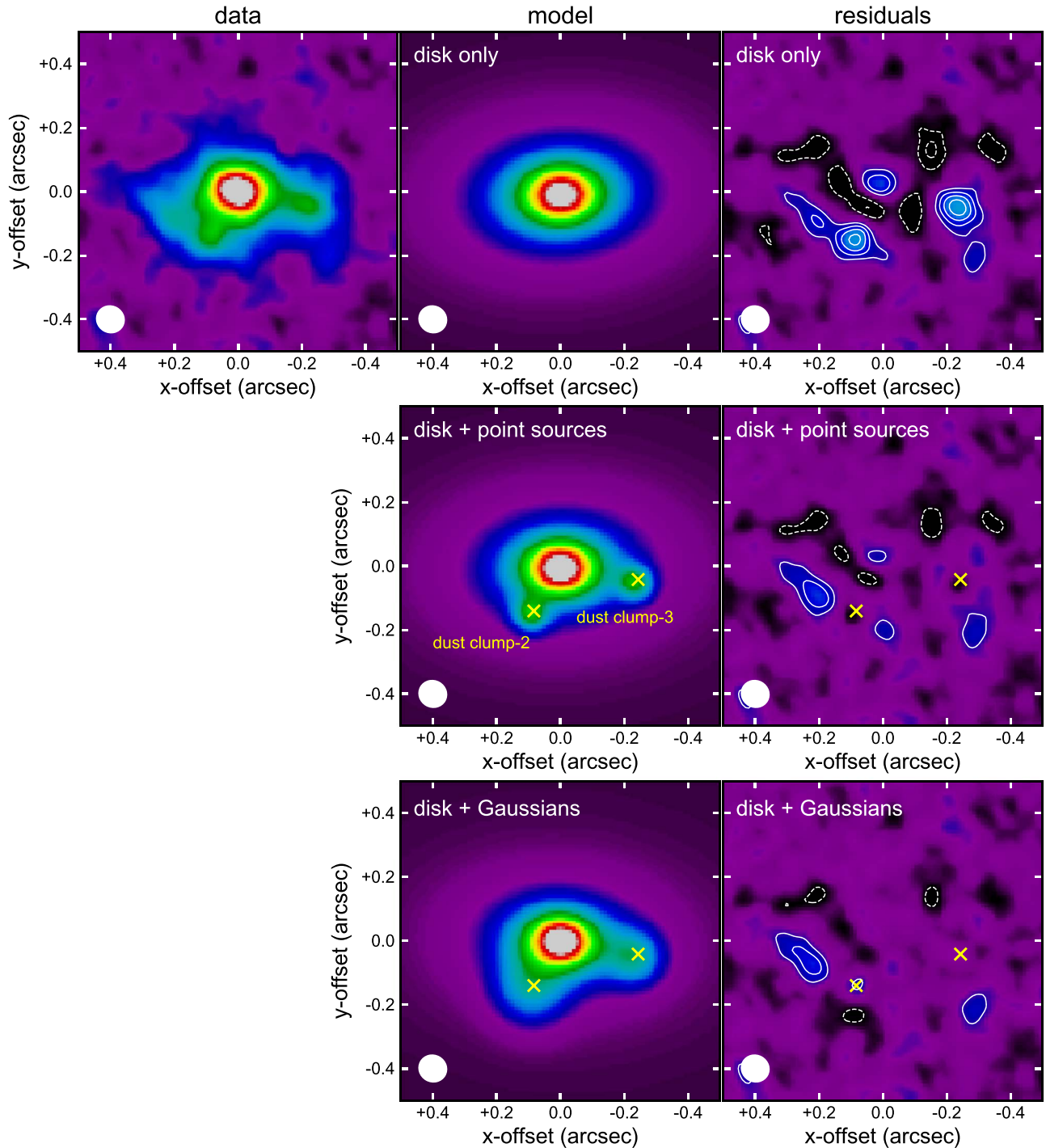


Figure 2. High-resolution ($0''.09$) ALMA images of $860\ \mu\text{m}$ continuum emission in COSMOS-AzTEC-1. From left to right, we show the clean map, the best-fit model and the residuals after subtracting the primary disk component. The image size is $1'' \times 1''$. We use three models: single Sérsic component (top), Sérsic + two point sources (middle), and Sérsic + two Gaussians (bottom). White contours show the -5 , -3 , 3 , 5 , 7 , 9σ levels in the residual maps. Yellow crosses mark the positions of two dust clumps.

of a rotating disk to the [C II] cube by using the `Galpak3D` code (Bouché et al. 2015). We assume a thick disk and an arctan rotation curve in the models. The models have nine free parameters: centroid position, systemic velocity, line flux S_{dv} , maximum rotation velocity V_{max} , local velocity dispersion σ_0 (not central velocity dispersion, but isotropic and constant one over the disk), half-light radius $R_{1/2}$, turnover radius, inclination, and position angle. Disk models with these parameters are convolved with the clean beam and are fitted

to the data cube using a Markov Chain Monte Carlo algorithm. We derive $S_{dv} = 13.31 \pm 0.32\ \text{Jy km s}^{-1}$, $V_{\text{max}} = 219 \pm 9\ \text{km s}^{-1}$, $\sigma_0 = 74 \pm 2\ \text{km s}^{-1}$, and $R_{1/2} = 1.76 \pm 0.13\ \text{kpc}$, where the systematic and random errors are taken into account on the basis of the simulations in a similar way as dust continuum observations (see Appendix B). The kinematic parameters agree well with those derived from the previous fitting of a $0.3''$ -resolution [C II] cube with a channel width of $50\ \text{km s}^{-1}$ (Tadaki et al. 2019), implying that measurements of

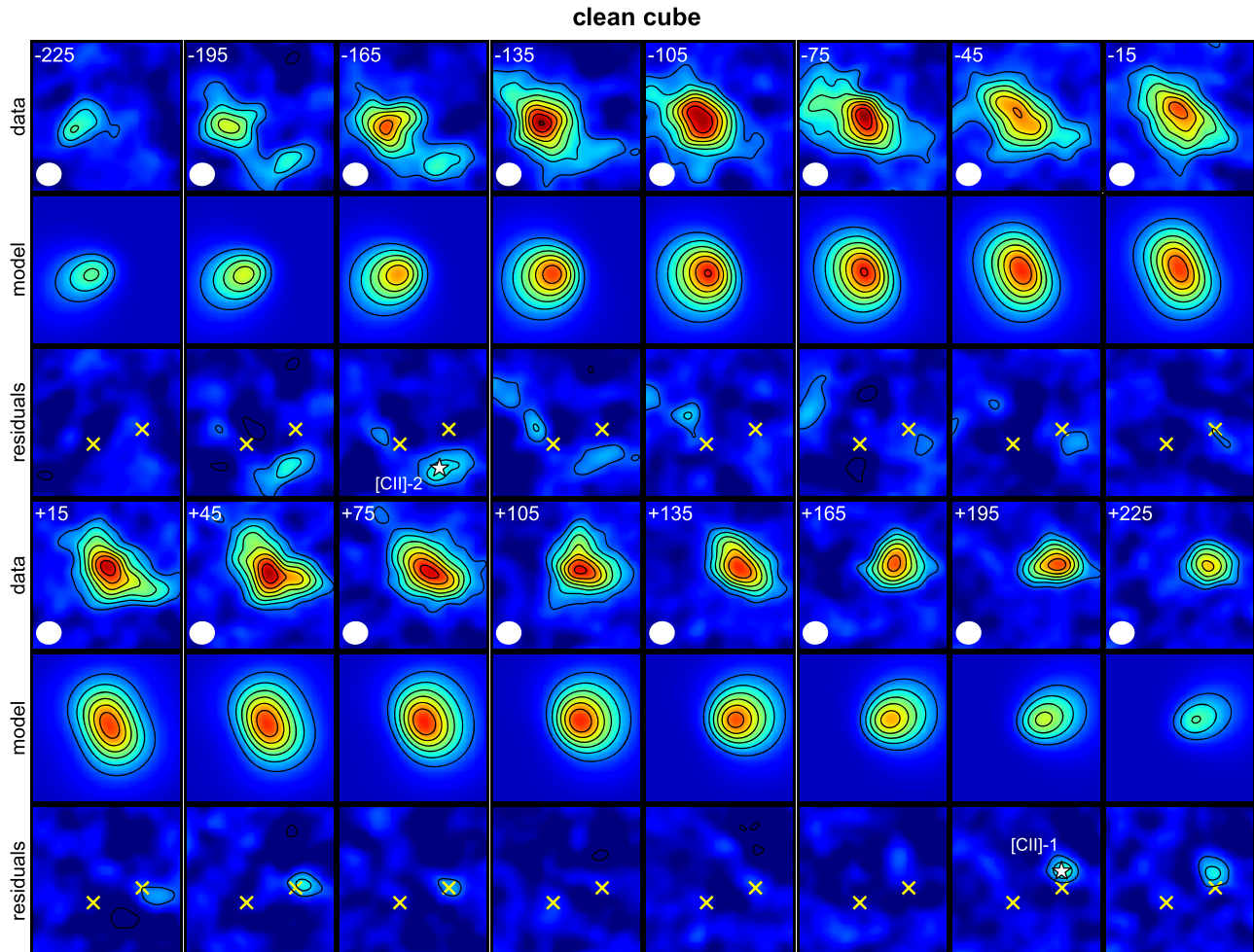


Figure 3. From top to bottom, the low-resolution ($0''.17$) [C II] channel maps, the best-fit models and the residuals are shown in the velocity range from -225 km s^{-1} to $+225 \text{ km s}^{-1}$. The image size is $1'' \times 1''$. Contours are plotted every 2σ from 3σ . Stars and crosses mark the positions of [C II] subcomponents and dust clumps, respectively.

maximum rotation velocity and local velocity dispersion do not require very high-resolution observations even in compact SMGs. This is thanks to the fact that the [C II] emission is relatively extended compared to the dust continuum and CO line emission (Gullberg et al. 2018; Tadaki et al. 2019). Given that [C II] emission is completely resolved out in $0''.05$ -resolution cubes created from only the extended configuration data (Iono et al. 2016), super-high-resolution observations of [C II] emission are risky. In the residual channel maps after subtraction of a smooth disk (Figure 3), two subcomponents ([C II]-1 and [C II]-2) are detected at above 5σ in two adjacent channels, corresponding to the detection significance of $\sim 7\sigma$ ($=5\sigma \times \sqrt{2}$) as the two channels are independent. Both observing simulations and analysis of a dirty cube demonstrate that these residual components are not artificially created by noise fluctuations and beam deconvolution (see Appendix B and Appendix C).

3.3. Properties of the Off-center Components

Figure 4 shows the [C II] spectra of the best-fit disk models and the residuals at the position of the two subcomponents. For [C II]-1, the peak velocity of the residual emission is consistent within a range of $\sim 100 \text{ km s}^{-1}$ from the coherent velocity of

the primary disk component, which is derived from single Gaussian fitting of the model spectrum. Such a corotation is naturally expected if this component is formed through gravitational instability in the rotating starburst disk. We note that a deviation from the idealized profile of the disk can possibly make such a corotating subcomponent, especially along the major axis of disk. For example, an asymmetric disk or shocks could artificially produce a subcomponent in the residuals, which in that case would simply represent part of the disk emission. It requires deeper observations to distinguish whether or not [C II]-1 truly represents a separate component from the overall disk rotation. On the other hand, [C II]-2 has a velocity offset of $\sim 200 \text{ km s}^{-1}$ from the coherent velocity of the disk, meaning that it does not corotate with the starburst disk. [C II]-2 is also located along the kinematic minor axis while [C II]-1 is located along the major axis (Figure 1). The spatial and velocity offset suggest that [C II]-2 is falling into COSMOS-AzTEC-1 from a direction perpendicular to the disk rotation.

We measure the [C II] flux of the off-center components in the velocity range where the emission is detected at above 2σ (Figure 4). In the low-resolution velocity-integrated maps, the peak flux is $0.147 \pm 0.017 \text{ Jy km s}^{-1} \text{ beam}^{-1}$ (8.6σ) for [C II]-1 and $0.186 \pm 0.022 \text{ Jy km s}^{-1} \text{ beam}^{-1}$ (8.4σ) for [C II]-2.

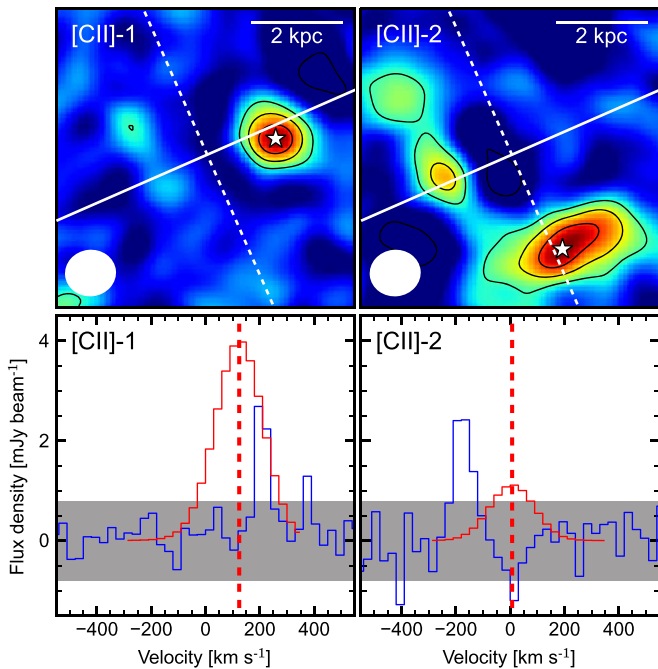


Figure 4. Spectra at the position of [C II] subcomponents, extracted from the low-resolution cube. Red and blue lines indicate the best-fit model as the primary disk component and the residuals between the data and the model, respectively. Gray shaded regions denote the 2σ level. Red vertical lines show the coherent velocity of the disk component at the position of subcomponents. The velocity-integrated residual maps are shown in the top panels. The image size is $1'' \times 1''$. Contours are plotted every 2σ from 3σ . White solid and dashed lines show the kinematic major and minor axis of disk rotation, respectively (Figure 1).

On the other hand, the peak flux in the high-resolution maps decreases to $0.087 \pm 0.021 \text{ Jy km s}^{-1} \text{ beam}^{-1}$ (4.2σ) for [C II]-1 and $0.113 \pm 0.026 \text{ Jy km s}^{-1} \text{ beam}^{-1}$ (4.4σ) for [C II]-2, indicating that these components are spatially extended. Therefore, we refer to these off-center components as a subcomponent rather than a clump. We derive $0.17 \pm 0.04 \text{ Jy km s}^{-1}$ for [C II]-1 and $0.62 \pm 0.10 \text{ Jy km s}^{-1}$ for [C II]-2 by using CASA/imfit, which fits an elliptical Gaussian component on the image. [C II]-1 and [C II]-2 contribute 1% and 4% to the total [C II] flux, respectively. These two [C II] subcomponents are not detected in dust emission while two dust clumps are not detected in [C II] emission. This result indicates that there are variations in the ratio of [C II] to far-infrared (FIR) luminosity of clumps and subcomponents. [C II] subcomponents tend to have a larger [C II]/FIR ratio than the clumps identified by dust continuum emission. In the [C II] subcomponents, molecular gas would not be irradiated by a strong far-ultraviolet field produced by massive stars in contrast to the dust clumps and central region of starburst disks (Rybak et al. 2019; Tadaki et al. 2019).

4. Discussion

By exploiting the high-quality [C II] line cube, we have identified two [C II] subcomponents in a bright SMG at $z = 4.3$, COSMOS-AzTEC-1. [C II]-2 has a large velocity offset of 200 km s^{-1} from the primary disk component while the peak velocity of [C II]-1 is consistent with that of the disk. The escape velocity from the galaxy is expected to be $\sim 500 \text{ km s}^{-1}$ at the position of [C II]-2, given that the [C I]-based gas mass of $7.2 \times 10^{10} M_{\odot}$ is mostly enclosed inside a

radius of 2.5 kpc (Tadaki et al. 2018). [C II]-2 could therefore come back to the galaxy even if it is temporarily going away. If we assume that [C II] flux ratios reflect mass ratios between the subcomponents and the starburst disk, [C II]-2 would be at least 10 times less massive than the disk component, which is also supported by non-detection of dust continuum emission. The physical separation between the primary disk component and [C II]-2 is 2 kpc, which has not been probed by previous low-resolution (over kpc scales) observations of gas. Pavesi et al. (2018) have also identified a [C II] subcomponent with a close separation of 2 kpc around a dusty starburst galaxy at $z = 5.67$. As the integration time of our ALMA observations is only 1 hr, it would be desirable to make similar observations in a large sample of unlensed bright SMGs to investigate whether they commonly have such a subcomponent within the disk.

The large velocity offset and the close separation suggest that COSMOS-AzTEC-1 not only undergoes a gas-rich minor merger, but also that the accreted gas component does not corotate with the disk, which could possibly behave like counter-rotating streams (Danovich et al. 2015). Since gas is not collisionless, unlike stars, it can effectively lose the angular momentum by dissipative processes. When a gaseous component with a different angular momentum is accreted into a rotating disk of the host galaxy, it could stimulate violent disk instability (VDI) where the disk is turbulent and highly perturbed, driving gas inflow into the central region of the galaxy (Dekel et al. 2009; Dekel & Burkert 2014; Zolotov et al. 2015). We suggest a scenario where the ex situ noncorotating subcomponent develops the VDI. The VDI-driven gas inflow can explain the observed central concentration of the CO(4–3) emission with a half-light radius of $R_{1/2} = 1.2 \text{ kpc}$ (Tadaki et al. 2019). In the central gaseous disk with a high gas mass surface density, in situ clumps can be formed through standard Toomre instability (Toomre 1964) or nonlinear VDI (Inoue et al. 2016) and are gravitationally bound against tidal forces and stellar feedback (Tadaki et al. 2018).

At the moment, it is not clear whether the accretion of only one small noncorotating gas component drastically affects the angular momentum and the spatial structure of gas in much more massive galaxies. We may need to consider the accretion of multiple gas-rich components with different angular momentum. For low gas fraction cases, multiple minor mergers with 1:50 can significantly change the morphology and the kinematics of massive galaxies (Bournaud et al. 2007). It should be verified by numerical simulations whether multiple minor mergers with high gas fraction drive radial gas inflows into the center of galaxies.

On the other hand, our finding of a noncorotating gas component does not necessarily reject the possibility that COSMOS-AzTEC-1 experiences another major merger in the past, which is an important mechanism to explain extreme starbursts with star-formation rate $\sim 1000 M_{\odot} \text{ yr}^{-1}$ (e.g., Hayward et al. 2013; Cibinel et al. 2019) and/or clump formation at high-redshift (Calabrò et al. 2019). Recent observations discover a group of ~ 10 gas-rich galaxies within 200–300 kpc around a bright SMG at $z \sim 4$ (Miller et al. 2018; Oteo et al. 2018, see also Capak et al. 2011; Hodge et al. 2013; Brisbin et al. 2017; Wardlow et al. 2018; Casey et al. 2019 for discoveries of gas-rich companions around dusty star-forming galaxies at high-redshift). In such high-density environments, gas-rich major mergers are naturally expected to occur and then trigger an extreme starburst in

the central galaxy of protoclusters. We do not detect other 1.1 mm continuum sources with $S_{1.1\text{mm}} > 100 \mu\text{Jy}$ per $0''.3$ beam within 80 kpc around COSMOS-AzTEC-1 (Tadaki et al. 2019) while there is an overdensity of optically selected galaxies with photometric redshift of $4.08 < z_{\text{phot}} < 4.60$ (Smolčić et al. 2017). The absence of 1.1 mm continuum sources does not positively support that previous major mergers drive gas inflows into the galaxy center.

Studying stellar kinematics is one of the most effective ways to validate the major merger scenario. Gas kinematics become rotation-dominated in both cases of major and minor mergers (Robertson et al. 2006 for numerical simulations, Ueda et al. 2014 for observations of CO lines) while only major mergers leave a dispersion-dominated stellar component with $V_{\text{rot}}/\sigma_0 < 1$ (Robertson et al. 2006 for simulations, Rothberg & Joseph 2006 for observations of Ca triplet lines). Bright SMGs are faint at $< 2 \mu\text{m}$ but relatively bright at 3–4 μm with an AB magnitude of 22. Integral field spectroscopy with the Near Infrared Spectrograph on *James Webb Space Telescope* (JWST; Dorner et al. 2016) will enable us to spatially resolve the stellar continuum and the absorption lines at kpc-resolution. Investigating both gas and stellar kinematics through ALMA-JWST synergetic observations will shed light on the physical mechanism responsible for extreme starbursts in the early universe.

We are very grateful to the referee for constructive suggestions to improve the paper. This paper makes use of the following ALMA data: ADS/JAO.ALMA#2015.1.01345.S, 2017.1.00127.S. ALMA is a partnership of ESO (representing its member states), NSF (USA), and NINS (Japan), together with NRC (Canada) and NSC and ASIAA (Taiwan) and KASI (Republic of Korea), in cooperation with the Republic of Chile. The Joint ALMA Observatory is operated by ESO, AUI/NRAO and NAOJ. K.T. acknowledges support by Grant-in-Aid for JSPS Research Fellow JP17J04449. Data analysis was in part carried out on the common-use data analysis computer system at the Astronomy Data Center (ADC) of the National Astronomical Observatory of Japan. This research made use of FAKEOBS, a software tool developed by the Nordic ALMA Regional Center. The Nordic ARC node is funded through Swedish Research Council grant No 2017-00648.

Appendix A

A Comparison Between Compact and Extended Array Configuration Data

We merge two array configuration data with different uv coverage in this work. To cross-check the flux scale between two data sets, we calculate the amplitudes of the vector-averaged visibilities as a function of uv distance in each array configuration (Figure 5). The errors are calculated from the standard deviations of the real and the imaginary part of visibilities in each bin of uv distance. Although there is no systematic offset between the visibility amplitudes, we see a small discrepancy between both data sets at 100–400 $k\lambda$, corresponding to the physical scale of the starburst disk in COSMOS-AzTEC-1. For the extended configuration data, the errors may be larger in this range due to the sparse uv coverage. The compact configuration data, homogeneously covering the uv plane, has an important role in characterizing the spatial extent of the kpc-scale disk.

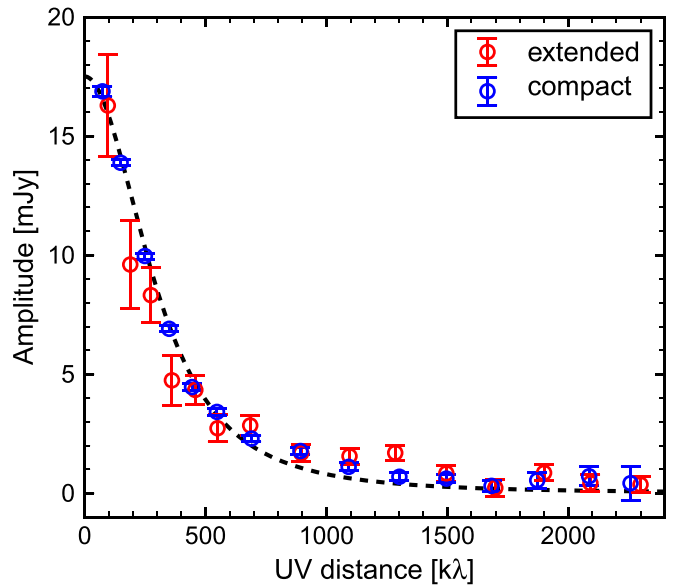


Figure 5. Visibility amplitudes vs. uv distances for 860 μm continuum in COSMOS-AzTEC-1. Red and blue symbols denote the data in the extended and compact array configurations, respectively. We overlay an exponential disk model with $S_{860} = 17.5$ mJy and a circularized half-light radius ($R_{1/2,\text{circ}} = R_{1/2}\sqrt{q}$) of 1.0 kpc as a reference.

APPENDIX C

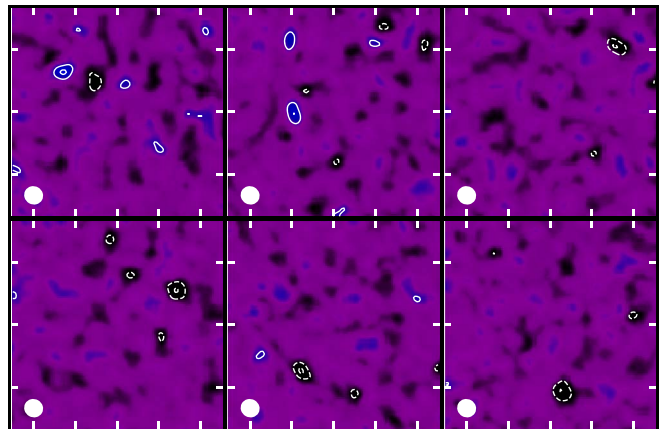


Figure 6. Six simulated residual maps showing positive or negative 5σ emission. The image size is $1'' \times 1''$. The contours are the same as in Figure 2.

Appendix B

Simulations of ALMA Observations

In Section 3.1, we identify the residual components after subtracting the best-fit model of a primary disk component in the 860 μm continuum map. To evaluate the significance of the residual emission as well as to estimate the realistic uncertainties on the best-fit parameters, we simulate ALMA observations of 860 μm continuum observations by using FAKEOBS, a software tool developed by the Nordic ALMA Regional Center. The input model is a smooth disk with Sérsic profile, which is derived from the single component fit of the 860 μm map in Section 3.1. We generate model visibilities with the same UV sampling as the observations, resulting in the same spatial resolution in clean images. We add noise to visibilities so that the simulated images have the same noise as in the observed ones. We also made two additional input models with a 20% larger and a 20% smaller size.

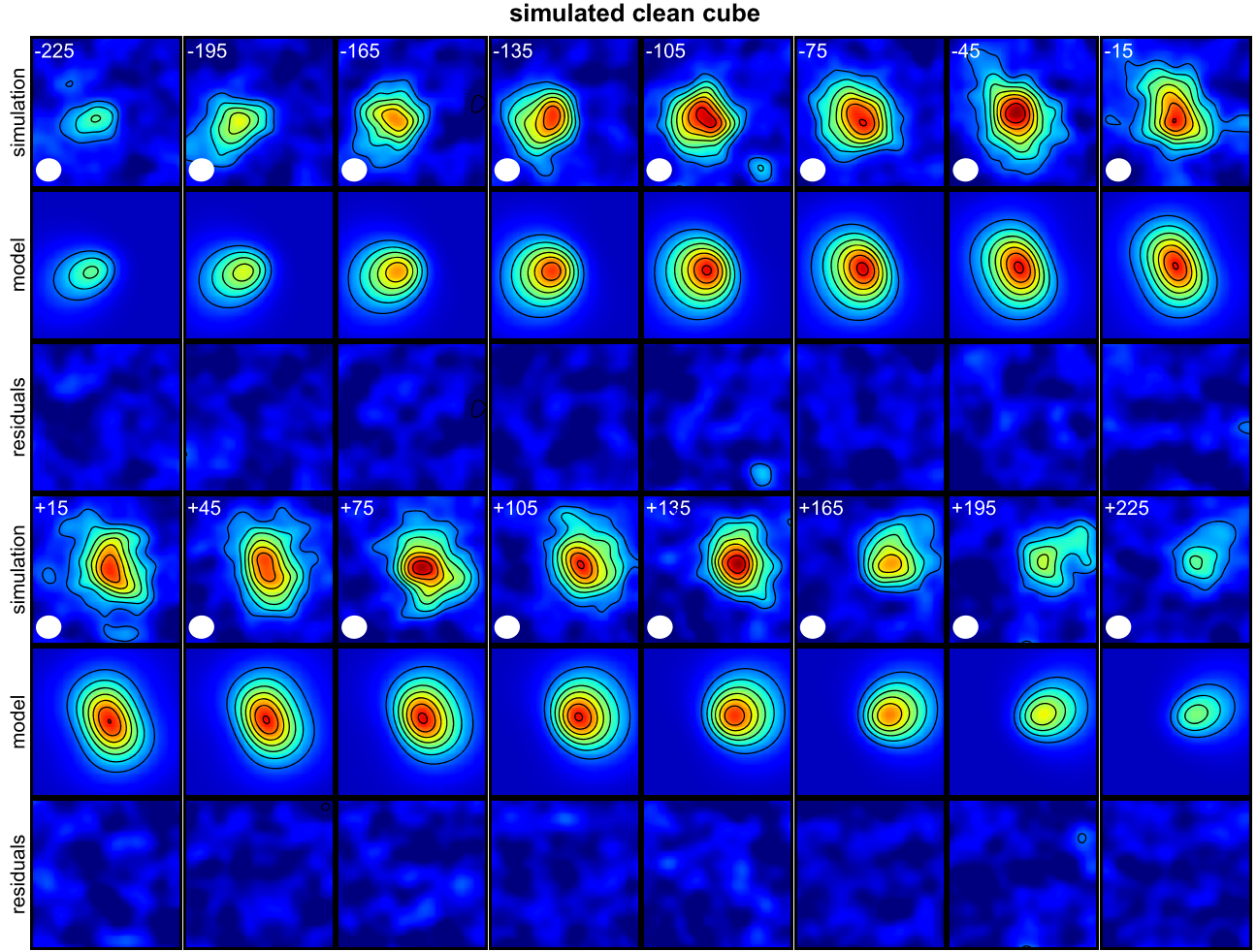


Figure 7. Same as Figure 3, but for a simulated clean cube of a smooth rotating disk, which is derived in Section 3.2. The contours and color coding are also the same as Figure 3.

We run the simulations 100 times with different seed numbers for noise generation in each model. Then, we fit Sérsic models to a total of 300 simulated high-resolution $860\ \mu\text{m}$ maps by using GALFIT. After subtracting the best-fit model, we search for residual emission within the central region with a radius of $0''.6$ of the 300 simulated residual maps show positive or negative 5σ emission (Figure 6). Therefore, there is 2% chance that 5σ residual emission is artificially created even in a smooth disk. The maximum peak by noise fluctuations is 5.3σ . We compare between the input and output parameters in the 300 simulations to evaluate the uncertainties. We obtain the median and standard deviation of $R_{1/2,\text{in}}/R_{1/2,\text{out}} = 0.92 \pm 0.06$, $S_{860,\text{in}}/S_{860,\text{out}} = 0.94 \pm 0.04$, $n_{\text{in}}/n_{\text{out}} = 0.91 \pm 0.06$, and $q_{\text{in}}/q_{\text{out}} = 1.02 \pm 0.03$. These systematic and random errors are taken into account throughout this work.

We also generate simulated visibilities by using the best-fit models of a disk plus two point sources and a disk plus two Gaussians, shown in Figure 2. From 100 simulations with a disk plus two point sources, we obtain $R_{1/2,\text{in}}/R_{1/2,\text{out}} = 0.90 \pm 0.04$, $S_{860,\text{in}}/S_{860,\text{out}} = 0.94 \pm 0.03$, $n_{\text{in}}/n_{\text{out}} = 0.91 \pm 0.06$, and $q_{\text{in}}/q_{\text{out}} = 1.03 \pm 0.03$ for a disk, $S_{860,\text{in}}/S_{860,\text{out}} = 1.04 \pm 0.13$ for dust clump-2 and $S_{860,\text{in}}/S_{860,\text{out}} = 1.05 \pm 0.11$ for dust clump-3. From 100 simulations with a disk plus two Gaussians, we obtain $R_{1/2,\text{in}}/R_{1/2,\text{out}} = 0.90 \pm 0.07$, $S_{860,\text{in}}/S_{860,\text{out}} = 0.93 \pm 0.05$, $n_{\text{in}}/n_{\text{out}} = 0.90 \pm 0.08$, and $q_{\text{in}}/q_{\text{out}} = 1.03 \pm 0.05$ for a

disk, $R_{1/2,\text{in}}/R_{1/2,\text{out}} = 0.98 \pm 0.11$ and $S_{860,\text{in}}/S_{860,\text{out}} = 1.01 \pm 0.15$ for dust clump-2, and $R_{1/2,\text{in}}/R_{1/2,\text{out}} = 1.06 \pm 0.14$ and $S_{860,\text{in}}/S_{860,\text{out}} = 1.09 \pm 0.14$ for dust clump-3.

In a similar way as the continuum observations, we make CASA simulations for line observations by using smooth rotating disk models with the same parameters derived in Section 3.2. We make 100 simulated clean cubes with a channel width of $30\ \text{km s}^{-1}$. We also change the size of the input model by $\pm 20\%$, resulting in a total of 300 simulated cubes. We fit kinematic models to the simulated cubes by using Galpak3D and subtract the best-fit model. In the 300 simulated cubes within the central region with a radius of $0''.5$, we do not detect residual emission at above 5σ in the velocity range of $\pm 300\ \text{km s}^{-1}$. The worst case is shown in Figure 7, where the maximum peak is detected at 4.9σ . In the wider sky regions with annular radius of $1''.0$ and $9''$ in the velocity range of $\pm 570\ \text{km s}^{-1}$, 5σ peaks are artificially created, but the fraction is only 0.004% of all pixels. The worst case in the 300 simulated cubes is a negative 6.7σ peak. However, none of them are associated with another 5σ peak in the adjacent channel. This indicates that $5\text{--}6\sigma$ significance in single channel is not a sufficient criterion for blind search of [C II] emission although our focus is a small targeted region. The comparisons between the input and output parameters give $Sdv_{\text{in}}/Sdv_{\text{out}} = 0.95 \pm 0.02$, $V_{\text{max,in}}/V_{\text{max,out}} = 0.96 \pm 0.04$, $\sigma_{0,\text{in}}/\sigma_{0,\text{out}} = 0.99 \pm 0.03$, and $R_{1/2,\text{in}}/R_{1/2,\text{out}} = 0.96 \pm 0.07$.

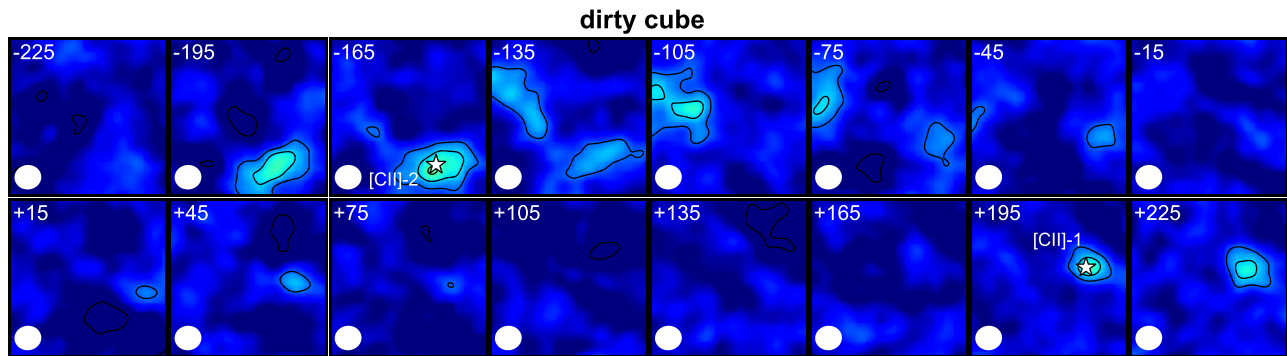


Figure 8. Dirty channel maps after subtracting the best-fit model. The contours and color coding are also the same as Figure 3.

Appendix C Analysis of Dirty Images

Another reason to create artifacts of residual emission is deconvolution of the dirty beam in the clean process. Noises could be potentially amplified by deconvolution if the cleaning is not perfect. We make the same analysis of a dirty cube to check if the results do not depend on being clean (Rujopakarn et al. 2019). Figure 8 shows residual channel maps of the dirty cube. Both [C II]-1 and [C II]-2 are detected at above 5σ in two channels, indicating that these residual emission are not enhanced by beam deconvolution when clean.

ORCID iDs

Ken-ichi Tadaki <https://orcid.org/0000-0001-9728-8909>
 Daisuke Iono <https://orcid.org/0000-0002-2364-0823>
 Min S. Yun <https://orcid.org/0000-0001-7095-7543>
 Itziar Aretxaga <https://orcid.org/0000-0002-6590-3994>
 Bunyo Hatsukade <https://orcid.org/0000-0001-6469-8725>
 Minju M. Lee <https://orcid.org/0000-0002-2419-3068>
 Tomonari Michiyama <https://orcid.org/0000-0003-2475-7983>
 Kouichiro Nakanishi <https://orcid.org/0000-0002-6939-0372>
 Toshiki Saito <https://orcid.org/0000-0002-2501-9328>
 Hideki Umehata <https://orcid.org/0000-0003-1937-0573>

References

- Aravena, M., Hodge, J. A., Wagg, J., et al. 2014, *MNRAS*, 442, 558
 Bolatto, A. D., Leroy, A. K., Rosolowsky, E., Walter, F., & Blitz, L. 2008, *ApJ*, 686, 948
 Bouché, N., Carfantan, H., Schroetter, I., Michel-Dansac, L., & Contini, T. 2015, *AJ*, 150, 92
 Bournaud, F., Jog, C. J., & Combes, F. 2007, *A&A*, 476, 1179
 Brisbin, D., Miettinen, O., Aravena, M., et al. 2017, *A&A*, 608, A15
 Calabrò, A., Daddi, E., Fensch, J., et al. 2019, *A&A*, 632, A98
 Capak, P. L., Riechers, D., Scoville, N. Z., et al. 2011, *Natur*, 470, 233
 Casey, C. M., Narayanan, D., & Cooray, A. 2014, *PhR*, 541, 45
 Casey, C. M., Zavala, J. A., Aravena, M., et al. 2019, *ApJ*, 887, 55
 Cibinel, A., Daddi, E., Sargent, M. T., et al. 2019, *MNRAS*, 485, 5631
 Cornwell, T. J. 2008, *ISTSP*, 2, 793
 Daddi, E., Dannerbauer, H., Stern, D., et al. 2009, *ApJ*, 694, 1517
 Daddi, E., Renzini, A., Pirzkal, N., et al. 2005, *ApJ*, 626, 680
 Damjanov, I., Abraham, R. G., Glazebrook, K., et al. 2011, *ApJL*, 739, L44
 Danovich, M., Dekel, A., Hahn, O., Ceverino, D., & Primack, J. 2015, *MNRAS*, 449, 2087
 De Breuck, C., Williams, R. J., Swinbank, M., et al. 2014, *A&A*, 565, A59
 Dekel, A., Birnboim, Y., Engel, G., et al. 2009, *Natur*, 457, 451
 Dekel, A., & Burkert, A. 2014, *MNRAS*, 438, 1870
 Dorner, B., Giardino, G., Ferruit, P., et al. 2016, *A&A*, 592, A113
 Elmegreen, B. G., & Elmegreen, D. M. 2005, *ApJ*, 627, 632
 Fensch, J., Renaud, F., Bournaud, F., et al. 2017, *MNRAS*, 465, 1934
 Fisher, D. B., Glazebrook, K., Abraham, R. G., et al. 2017, *ApJL*, 839, L5
 Fujimoto, S., Ouchi, M., Kohno, K., et al. 2018, *ApJ*, 861, 7
 Genzel, R., Newman, S., Jones, T., et al. 2011, *ApJ*, 733, 101
 Gullberg, B., Swinbank, A. M., Smail, I., et al. 2018, *ApJ*, 859, 12
 Hayward, C. C., Narayanan, D., Kereš, D., et al. 2013, *MNRAS*, 428, 2529
 Heyer, M., & Dame, T. M. 2015, *ARA&A*, 53, 583
 Hodge, J. A., Carilli, C. L., Walter, F., et al. 2012, *ApJ*, 760, 11
 Hodge, J. A., Carilli, C. L., Walter, F., Daddi, E., & Riechers, D. 2013, *ApJ*, 776, 22
 Hodge, J. A., Smail, I., Walter, F., et al. 2019, *ApJ*, 876, 130
 Hodge, J. A., Swinbank, A. M., Simpson, J. M., et al. 2016, *ApJ*, 833, 103
 Hopkins, P. F., Hernquist, L., Cox, T. J., et al. 2006, *ApJS*, 163, 1
 Ikarashi, S., Ivison, R. J., Caputi, K. I., et al. 2015, *ApJ*, 810, 133
 Inoue, S., Dekel, A., Mandelker, N., et al. 2016, *MNRAS*, 456, 2052
 Iono, D., Yun, M. S., Aretxaga, I., et al. 2016, *ApJL*, 829, L10
 Ivison, R. J., Smail, I., Amblard, A., et al. 2012, *MNRAS*, 425, 1320
 Ivison, R. J., Swinbank, A. M., Smail, I., et al. 2013, *ApJ*, 772, 137
 Jogee, S., Miller, S. H., Penner, K., et al. 2009, *ApJ*, 697, 1971
 Kaviraj, S. 2014, *MNRAS*, 437, L41
 Kaviraj, S., Peirani, S., Khochfar, S., Silk, J., & Kay, S. 2009, *MNRAS*, 394, 1713
 Larson, K. L., Sanders, D. B., Barnes, J. E., et al. 2016, *ApJ*, 825, 128
 Lin, L., Koo, D. C., Willmer, C. N. A., et al. 2004, *ApJL*, 617, L9
 Litke, K. C., Marrone, D. P., Spilker, J. S., et al. 2019, *ApJ*, 870, 80
 McMullin, J. P., Waters, B., Schiebel, D., Young, W., & Golap, K. 2007, in ASP Conf. Ser. 376, *Astronomical Data Analysis Software and Systems XVI*, ed. R. A. Shaw, F. Hill, & D. J. Bell (San Francisco, CA: ASP), 127
 Miller, T. B., Chapman, S. C., Aravena, M., et al. 2018, *Natur*, 556, 469
 Newman, S. F., Shapiro Griffin, K., Genzel, R., et al. 2012, *ApJ*, 752, 111
 Oteo, I., Ivison, R. J., Dunne, L., et al. 2018, *ApJ*, 856, 72
 Pavesi, R., Riechers, D. A., Sharon, C. E., et al. 2018, *ApJ*, 861, 43
 Peng, C. Y., Ho, L. C., Impey, C. D., & Rix, H.-W. 2010, *AJ*, 139, 2097
 Riechers, D. A., Carilli, C. L., Capak, P. L., et al. 2014, *ApJ*, 796, 84
 Robertson, B., Bullock, J. S., Cox, T. J., et al. 2006, *ApJ*, 645, 986
 Rothberg, B., & Joseph, R. D. 2006, *AJ*, 132, 976
 Rujopakarn, W., Daddi, E., Rieke, G. H., et al. 2019, *ApJ*, 882, 107
 Rybak, M., Calistro Rivera, G., Hodge, J. A., et al. 2019, *ApJ*, 876, 112
 Sanders, D. B., Soifer, B. T., Elias, J. H., et al. 1988, *ApJ*, 325, 74
 Simpson, J. M., Smail, I., Swinbank, A. M., et al. 2015, *ApJ*, 799, 81
 Smolčić, V., Miettinen, O., Tomičić, N., et al. 2017, *A&A*, 597, A4
 Starkenburg, T. K., Helmi, A., & Sales, L. V. 2016, *A&A*, 587, A24
 Swinbank, A. M., Dye, S., Nightingale, J. W., et al. 2015, *ApJL*, 806, L17
 Tacconi, L. J., Genzel, R., Smail, I., et al. 2008, *ApJ*, 680, 246
 Tadaki, K., Iono, D., Yun, M. S., et al. 2018, *Natur*, 560, 613
 Tadaki, K.-i., Iono, D., Hatsukade, B., et al. 2019, *ApJ*, 876, 1
 Toft, S., Smolčić, V., Magnelli, B., et al. 2014, *ApJ*, 782, 68
 Toomre, A. 1964, *ApJ*, 139, 1217
 Trujillo, I., Feulner, G., Goranova, Y., et al. 2006, *MNRAS*, 373, L36
 Ueda, J., Iono, D., Yun, M. S., et al. 2014, *ApJS*, 214, 1
 Valentino, F., Tanaka, M., Davidzon, I., et al. 2019, arXiv:1909.10540
 van Dokkum, P. G., Nelson, E. J., Franx, M., et al. 2015, *ApJ*, 813, 23
 Wardlow, J. L., Simpson, J. M., Smail, I., et al. 2018, *MNRAS*, 479, 3879
 Younger, J. D., Fazio, G. G., Wilner, D. J., et al. 2008, *ApJ*, 688, 59
 Zolotov, A., Dekel, A., Mandelker, N., et al. 2015, *MNRAS*, 450, 2327